

Simulation of the Magnetization Dynamics of a Single Domain BiFeO₃ Thin Film

Yu-Ching Liao¹, Dmitri E. Nikonov², Sourav Dutta^{1,3}, Sou-Chi Chang², Sasikanth Manipatruni², Ian A. Young², and Azad Naeemi¹

¹School of Electrical and Computer Engineering, Georgia Institute of Technology, Atlanta, GA 30332 USA

²Components Research, Technology & Manufacturing Group Intel Corporation, Hillsboro, OR 97124 USA

³Department of Electrical Engineering, University of Notre Dame, Notre Dame, IN 46556, USA

Abstract:

The switching dynamics of a single-domain BiFeO₃ thin film is investigated through combining the dynamics of polarization and Neel vector. The evolution of the ferroelectric polarization is described by the Landau-Khalatnikov (LK) equation, and the Landau–Lifshitz–Gilbert (LLG) equations for spins in two sublattices to model the time evolution of the antiferromagnetic order (Neel vector) in a G-type antiferromagnet. This work theoretically demonstrates that due to the rotation of the magnetic hard axis following the polarization reversal, the Neel vector can be switched by 180°, while the weak magnetization can remain unchanged. The simulation results are consistent with the ab initio calculation¹, where the Neel vector rotates during polarization rotation, and also match our calculation of the dynamics of order parameter using Landau-Ginzburg theory². We also find that the switching time of the Neel vector is determined by the speed polarization switching and is predicted to be as short as 30 ps.

Introduction

Recently, the demand for low-power non-volatile devices has led a growing interest in beyond-CMOS spintronic devices. Among them, magnetoelectric (ME) devices are promising as they are voltage-driven and dissipate less energy compared to current-driven spintronic devices^{3,4}. However, the speed of the proposed ME devices are slower compared to the high performance CMOS^{5,6} transistors. Multiferroic materials showing at least two of the possible simultaneously occurring characteristics- ferroelectricity, ferromagnetism, antiferromagnetism, and ferroelasticity⁷ are promising for ME devices due to their intrinsic magnetoelectric coupling. In addition, ME devices using the exchange interaction between a ferromagnet and a multiferroic material exhibit deterministic 180° magnetization switching rather than 90° easy axis rotation typical for piezoelectric-magnetostrictive heterostructures. Recent calculations show that an antiferromagnet can switch on the order of 10 ps^{8,9}, much faster than the ferromagnet because of the strong exchange coupling and the characteristic of inertia-driven switching¹⁰. Bismuth ferrite, BiFeO₃, possessing ferroelectricity, G-type antiferromagnetism, and weak magnetization, is the

only single-phase multiferroic material known so far, that has both the Curie temperature ($T_c \sim 1103\text{K}$) and the Neel temperature ($T_N \sim 643\text{K}$) well above room temperature, which makes it a promising candidate for the room-temperature application. Currently, most experimental demonstrations^{1,11,12} and theoretical simulations^{13,14} regarding BiFeO_3 focus on the magnetic textures of BiFeO_3 under high magnetic field² or epitaxial strain¹⁵, the polarization switching time¹⁶, or the multidomain switching of $\text{BiFeO}_3/\text{CoFe}$ heterojunction^{12,13}. However, there are no comprehensive studies of the spin switching in BiFeO_3 considering its application in ultra-scaled beyond CMOS devices. Therefore, in this paper, we aim at analyzing the switching dynamics and the switching time of the magnetic order in a single-domain BiFeO_3 thin film after applying the electric field. We solve the magnetic order of BiFeO_3 by using the Landau-Ginzburg phenomenological theory to derive both LK and LLG equations. Our simulations of the magnetic dynamics show that the Neel vector switches 180° after the polarization reversal. We also verify the consistency of the results with those obtained via solving the effective equation of motion for the Neel vector.

Bulk BiFeO_3 has a rhombohedrally distorted perovskite structure and belongs to the space symmetry group $R3c$, while the crystal structure and space group in a thin film BiFeO_3 may vary from tetragonal to orthorhombic depending on the compressive or tensile strain¹⁷. The ferroelectricity of BiFeO_3 mostly originates from the displacement of Bi^{3+} ions relative to the rest of the lattice under an applied electric field. Thus, the application of a sufficiently strong applied electric field will reverse the polarization^{11,18}. Interestingly, during polarization reversal, the iron ions and oxygen octahedra also rotate, which causes the weak magnetization to rotate¹. The weak magnetization in BiFeO_3 originates from the Dzyaloshinskii-Moriya interaction (DMI)^{19,20}, which is due to the tilting of oxygen octahedra from the ideal ABO_3 perovskite structure combined with the spin-orbit coupling effect. The Hamiltonian of DMI is expressed as

$$E_{DMI} = \sum_{i=1}^N \sum_{j \neq i}^{nn} \mathbf{D}_{i,j} \cdot (\mathbf{S}_i \times \mathbf{S}_j), \quad (1)$$

where $\mathbf{D}_{i,j}$ is the DM vector between cells i and j , and \mathbf{S}_i and \mathbf{S}_j are the spin vectors of cells i and j , respectively. The direction of the DM vector is determined by the cross product of the displacement of oxygen ion \mathbf{x} from the midpoint between Fe ions and the distances between two Fe ions \mathbf{r}_{ij} so that $\mathbf{D}_{i,j} = V_0(\mathbf{r}_i \times \mathbf{r}_j) = V_0(\mathbf{r}_{ij} \times \mathbf{x})$ where V_0 is the microscopic constant. From a crystallographic point of view, the rotation of the oxygen octahedra is anti-phase when viewing from the rotation axis, which is also called anti-ferrodistortive axis \mathbf{AFD} , of BiFeO_3 ²¹. Hence, the displacement of oxygen ion, \mathbf{x} , and the DM vector $\mathbf{D}_{i,j}$ are both staggered vectors or quasi-axial vectors, and the direction of $\mathbf{D}_{i,j}$ is determined by the \mathbf{AFD} .²¹ Ab initio calculations¹ have shown that $\mathbf{D}_{i,j}$ is nearly parallel to the polarization during polarization rotation so that this ME coupling will determine the switching dynamics in our model. One can also re-write the Hamiltonian of DMI as

$$E_{DMI} \approx \sum_{i=1}^N \mathbf{D}_{i,j} \cdot (\mathbf{N} \times \mathbf{M}_c) = \mathbf{H}_{DMI} \cdot \sum_i \mathbf{S}_i^{AFM} \quad (2)$$

considering there are two sublattices A and B where $\mathbf{N} = \sum_{i,j} (\mathbf{S}_i^A - \mathbf{S}_j^B)$ is the Neel vector, $\mathbf{M}_c = \sum_{i,j} (\mathbf{S}_i^A + \mathbf{S}_j^B)$ is the weak-canted magnetization, and $\mathbf{H}_{DMI} = \mathbf{D}_{i,j} \times \mathbf{N}$ is the effective magnetic

field of DMI since the direction of $\mathbf{S}_i \times \mathbf{S}_j$ is equal to $\mathbf{N} \times \mathbf{M}_c$. Note that because of the cross-product relation between $\mathbf{D}_{i,j}$, \mathbf{N} , and \mathbf{M}_c , these three vectors always form a right-handed system²². We will later compare the results based on these two expressions of the DMI field to verify the equivalency.

Ferroelectric and magnetic dynamics simulation model

We aim to simulate the spin dynamics and the switching time of a single-domain area of BiFeO₃ thin film whose magnetization can be controlled by an external electric field. We focus on a single-domain BiFeO₃ thin film because of its potential application in beyond-CMOS devices scaled to nanometer sizes. Previous studies¹ have shown that the Bi³⁺ ion displacement, Fe ion displacement, and the tilting angles of oxygen octahedra have similar switching paths, which indicates that the ferroelectricity and weak ferromagnetism are coupled during switching, and the switching of the magnetization in BiFeO₃ can be determined by combining the ferroelectric and micromagnetic models. In other words, the axial vector $\mathbf{D}_{i,j}$ in the micromagnetic simulation can be modified by the polarization in each time step in the ferroelectric dynamics. Therefore, in this work, we simulate the dynamics of \mathbf{N} , and \mathbf{M}_c in a single-domain BiFeO₃ thin film following the rotation of polarization and $\mathbf{D}_{i,j}$ as shown in Figure 1.

The polarization (\mathbf{P}) dynamics of BiFeO₃ is described by the LK equation

$$\gamma_{FE} \frac{\partial \mathbf{P}_i}{\partial t} = - \frac{\partial F}{\partial \mathbf{P}_i}, \quad (3)$$

where γ_{FE} is the ‘viscosity coefficient’, and F is the total free energy of the ferroelectric. The simplified total free energy of the single-domain ferroelectric is expressed as²³:

$$F(\mathbf{P}, \boldsymbol{\varepsilon}) = \alpha_1(\mathbf{P}_1^2 + \mathbf{P}_2^2 + \mathbf{P}_3^2) + \alpha_{11}(\mathbf{P}_1^4 + \mathbf{P}_2^4 + \mathbf{P}_3^4) + \alpha_{12}(\mathbf{P}_1^2 \mathbf{P}_2^2 + \mathbf{P}_1^2 \mathbf{P}_3^2 + \mathbf{P}_2^2 \mathbf{P}_3^2) + K_{Strain}(\mathbf{P} \cdot \mathbf{u})^2 - (c \frac{(\mathbf{P}_{dw} - \mathbf{P}) \cdot \mathbf{P}}{\epsilon_r \epsilon_0} + \mathbf{P} \cdot \mathbf{E}_{ext}), \quad (4)$$

where $\alpha_1, \alpha_{11}, \alpha_{12}$ are the phenomenological Landau expansion coefficients, \mathbf{u} is the axis of substrate strain, K_{Strain} is the strain energy, c is the geometry factor of the averaged domain wall, $\mathbf{P}_1, \mathbf{P}_2$, and \mathbf{P}_3 are the polarization components in x, y , and z - directions, \mathbf{E}_{ext} is the external electric field. We take the case of intrinsic strain due to deposition to result in an easy plane normal to the $[0\ 1\ 1]^1$. The last term in (4) represents the depolarization energy and the external field energy, and \mathbf{P}_{dw} is the polarization in an adjacent domain. The depolarization energy is calculated by approximating the depolarization field due to bound charges as the difference between polarizations on the sides of the domain wall. Note that the ferroelectric domain wall here is considered as the averaged contribution to the single domain ferroelectric. We then assume an input pulse of the electric field with the duration of 80 ps and a rise time of 5 ps. With these assumptions, the trajectory of polarization switching, i.e. the two-steps polarization switching, is in agreement with the ab initio calculation¹ as will be shown later. The parameters of the ferroelectric model are listed in Table 1.

We start by using the Landau-Ginzburg (LG) theory to simulate the spin dynamics. Landau-Ginzburg theory^{15,2,24} usually describes the antiferromagnetic order of BiFeO₃ by a Neel

vector \mathbf{n} . Similar to the spin Hamiltonian discussed previously, \mathbf{n} and \mathbf{m} are microscopically defined as the vectors of the difference and the summation of the magnetic moment densities of the two sublattices in an antiferromagnet, respectively. The total free energy density of a BiFeO₃ thin film includes the homogeneous and inhomogeneous exchange energies $F_{exch} = a\mathbf{m}^2 + A\sum(\nabla\mathbf{n}_i)^2$, magnetic anisotropy energy $F_{an} = K_{AFM}(\mathbf{e}_p \cdot \mathbf{n})^2$, magnetoelastic energy $F_{M,elast} = K_{epi}(\mathbf{e}_s \cdot \mathbf{n})^2$, and DMI energy $F_{DMI} = X_{\perp}\mathbf{H}_{DMI}^2 \frac{(\mathbf{e}_p \cdot \mathbf{n})^2}{2}$ where a is the homogeneous exchange constant, A is the inhomogeneous exchange constant, K_{AFM} is the effective anisotropy energy which includes single-ion anisotropy energy and effective anisotropy energy that comes from DM interaction, \mathbf{e}_p is the hard axis of the antiferromagnet, K_{epi} is the anisotropy energy originates from epitaxial constraint, \mathbf{e}_s is the axis normal to the film, X_{\perp} is the magnetic susceptibility that is perpendicular to \mathbf{n} , and \mathbf{H}_{DMI} is the DM field. In our model, we assume the single-domain BiFeO₃ thin film has a homogeneous weak magnetization without spin cycloid such that F_{exch} vanishes; thus, only F_{an} , $F_{M,elast}$ and F_{DMI} are involved. By taking the derivative of magnetic free energy with respect to \mathbf{n} , we get the Neel field as:

$$\mathbf{f}_n \equiv -\delta_{\mathbf{n}}F = -X_{\perp}H_D^2(\mathbf{e}_p \cdot \mathbf{n})\mathbf{e}_p - 2K_{AFM}(\mathbf{e}_p \cdot \mathbf{n})\mathbf{e}_p - 2K_{epi}(\mathbf{e}_s \cdot \mathbf{n})\mathbf{e}_s, \quad (5)$$

The dynamics of \mathbf{n} is then solved by the effective equation of motion for the Neel field²⁵

$$\frac{\dot{\mathbf{n}}}{\tilde{\gamma}} = G_1\dot{\mathbf{f}}_n + a[\gamma\mathbf{f}_n - G_2\dot{\mathbf{n}}], \quad (6)$$

where $\tilde{\gamma}$ is the effective gyromagnetic ratio, G_1 and G_2 are the phenomenological Gilbert damping parameters.

To model both N and M_c of the antiferromagnet more accurately, we also use the micromagnetic simulation. Previous studies already demonstrated that the dynamics of an antiferromagnet using the Neel vector is the same as the dynamics of a micromagnet with two sublattices²⁶ where they both conclude the same equation of motion of the Neel vector. Therefore, we further describe a G-type antiferromagnet with two sublattices a and b , where the magnetization of one sublattice is antiparallel to another sublattice and the dynamics is solved separately for each cell. We will later calculate the time evolution of the order parameter \mathbf{n} to compare with the results solved by a micromagnet with two sublattices. The dynamics of a micromagnet is solved by the LLG equation in each cell and the time-varying polarization is assumed homogeneously distributed in the sample. We use both the Object Oriented MicroMagnetic Framework (OOMMF)²⁷ and our own numerical micromagnetic model based on the finite difference method to account for the microscale interactions such as exchange coupling and compare the results of the two different expressions of DMI. The dynamics of an antiferromagnet is obtained by calculating

$$\dot{\mathbf{M}}_i = -\gamma(\mathbf{M}_i \times \mathbf{H}_i) + \frac{\alpha_G}{M_s}(\mathbf{M}_i \times \dot{\mathbf{M}}_i), \quad (7)$$

where \mathbf{M}_i is the magnetization in cell i , \mathbf{H}_i is the effective local magnetic field in cell i , M_s is the saturation magnetization, and α_G is the Gilbert damping factor. In our model, $\mathbf{H}_i = \mathbf{H}_{ex,ij} + \mathbf{H}_{ani} + \mathbf{H}_{dem,i} + \mathbf{H}_{DMI}$ where $\mathbf{H}_{ex,ij}$ is the exchange coupling field from cell i to its six nearest

neighboring cells j , \mathbf{H}_{ani} is the anisotropy field composed of bulk anisotropy field from DMI and the anisotropy field that comes from compressive epitaxial constraint, $\mathbf{H}_{dem,i}$ is the demagnetization field in cell i , and \mathbf{H}_{DMI} is a magnetic field arising from DM interaction in our OOMMF model whereas in our own micromagnetic solver, the DM Hamiltonian is used. We will compare the differences in the later discussion. The numerical micromagnetic model considers the discretization of the field with each term in the effective field expressed as:

$$\mathbf{H}_{ex,ij} = \frac{2A_{AFM}}{\mu_0 M_s} \sum \frac{m(r_i - \Delta_j) - 2m(r_i) + m(r_i + \Delta_j)}{|\Delta_j^2|}, \quad (8)$$

$$\mathbf{H}_{ani} = \mathbf{H}_{ani,bulk} + \mathbf{H}_{ani,epi} = \frac{2K_{AFM}}{\mu_0 M_s} (\mathbf{m} \cdot \mathbf{P}) \cdot \mathbf{P} + \frac{2K_{EPI}}{\mu_0 M_s} \mathbf{m}_z, \quad (9)$$

$$\mathbf{H}_{DMI} = -\frac{1}{\mu_0 M_s} \frac{\partial E_{DMI}}{\partial \mathbf{m}_i} = -\frac{1}{\mu_0 M_s} \mathbf{M}_j \times \mathbf{D}_{i,j}, \quad (10)$$

$$\mathbf{H}_{dem,i} = \frac{-1}{4\pi} \int \frac{n \cdot \mathbf{M}(r')(r-r')}{|r-r'|^3} d^2 r' \quad (11)$$

integrating all the other cells besides cell i . The details of $\mathbf{H}_{dem,i}$ calculation are explained in ²⁸. Note that the polarization direction determines the hard axis of the bulk anisotropy field because $\mathbf{D}_{i,j}$ is a uniaxial vector that is parallel to polarization (\mathbf{P})²⁹, and the hard axis of compressive epitaxial constraint anisotropy field is along $[001]$ ^{15,24}. The schematic of the rotation of easy plane state during polarization reversal is shown in the experiment²⁹.

The simulation parameters in the micromagnetic model are listed in Table 2 ¹³. The negative sign of K_{AFM} and K_{EPI} refers to the magnetic easy plane state. The sample size of BiFeO₃ is 32 nm thick and 20 nm wide and long, and the mesh size is $5 \times 5 \times 1 \text{ nm}^3$.

Results and discussion

We analyze the switching dynamics of BiFeO₃ by introducing two unitless vector variables $\mathbf{N} = (\mathbf{M}_1 - \mathbf{M}_2)/(|\mathbf{M}_1| + |\mathbf{M}_2|)$ and $\mathbf{M}_c = (\mathbf{M}_1 + \mathbf{M}_2)/(|\mathbf{M}_1| + |\mathbf{M}_2|)$, which refer to the Neel vector and the weak-canted magnetization of the antiferromagnet, respectively. At the initial stage before the switching starts, Figure 2(a) shows that \mathbf{M}_c , which is calculated by averaging the magnetization of in every 1 nm of the thickness, is staggered in the x , y , and z directions particularly close to the surface. To understand the staggered behavior of \mathbf{M}_c close to the surface, note that within the bulk the anisotropy field and DM field are small compared to the antiferromagnetic exchange coupling field as each cell is surrounded by six nearest neighbors. The exchange coupling field for the surface cells, however, is caused by fewer neighboring cells. Because of the weaker exchange field, the spin vectors on the surface tilt more by the DM field compared to the cells in the bulk region as shown in Figure 2(b). However, since the exchange coupling field is a short-range order field, which becomes negligible to the second nearest neighbors, the staggered \mathbf{M}_c only occurs at the surface of the BiFeO₃. Conversely, the \mathbf{M}_c shows a net magnetization in the bulk region because the spin vectors are almost antiparallel to each other and the DM field creates a weak, unidirectional magnetization. The magnitude of DM field is calculated by comparing the value of \mathbf{M}_c with the saturation magnetization in the hysteresis loop of the BiFeO₃ thin film in

experiment³⁰. The peak value of \mathbf{M}_c is approximately 1.8×10^3 A/m, which corresponds to about 1000 Oe \mathbf{H}_{DMI} in our model in Figure 3.

Next, to understand the energy barrier and the preferred axis during polarization reversal, we plot the energy landscape considering bulk anisotropy energy and anisotropy energy that comes from epitaxial constraint in Figure 4. We define the polar angle between magnetization and x -axis as θ ; and the azimuthal angle between magnetization and the y -axis on the yz plane as φ . The results show that when $\mathbf{H}_{ani,epi}$ is larger than $\mathbf{H}_{ani,bulk}$, the lowest energy of magnetization lies on the xy plane, and the maximum energy barrier happens at $[0\ 0\ 1]$ and $[0\ 0\ -1]$. However, when $\mathbf{H}_{ani,bulk}$ is larger than $\mathbf{H}_{ani,epi}$, the preferred easy plane changes to $[1\ -1\ 1]$, where the hard axis is parallel to the polarization direction. Considering the superposition of $\mathbf{H}_{ani,bulk}$ and $\mathbf{H}_{ani,epi}$, the preferred easy axis becomes along $[1\ 1\ 0]$, which is consistent with the experiment results²⁹. This is because the epitaxial constraint lifts the preferred easy plane state and results in a unique easy axis state. Because of the rotation of the $\mathbf{H}_{ani,bulk}$ along with the polarization, the easy axis of BiFeO₃ rotates during polarization switching. Figure 4 also show that the energy barrier of magnetization switching in BiFeO₃ is small since the single-ion anisotropy energy from Fe is small when it is half-filled in d orbitals³¹.

We now study dynamics of \mathbf{P} , \mathbf{N} and \mathbf{M}_c in BiFeO₃ by applying a negative electric field $\mathbf{E}_{ext} = 3 \times 10^8$ A/m. Figure 5 demonstrates that the switching curves of \mathbf{P} matches qualitatively to the ab initio calculation in ¹, and \mathbf{N} switches 180° while \mathbf{M}_c remains in the same direction after the polarization switching. The switching curves of \mathbf{N} also show that \mathbf{N} would first rotate 90° to $[-1\ 1\ 0]$ and then rotate to $[1\ 1\ 0]$, which is consistent to the ab initio calculation results in ¹. Next, we find that both the LG theory, which solved the order parameter \mathbf{n} , and the OOMMF model, which solved for both \mathbf{N} and \mathbf{M}_c , show the same results that \mathbf{N} switches 180° during polarization reversal in Figure 5. This demonstrates that our micromagnetic model is consistent with the previous approaches that used LG theory^{2,15}. However, unlike LG theory, our micromagnetic model can describe canted magnetization (\mathbf{M}_c). Note that the final \mathbf{N} is not precisely along $[1\ 1\ 0]$ because in a BiFeO₃ thin film, the polarization will deviate from ideal $[1\ -1\ 1]$ in tetragonal lattice. Hence, \mathbf{N} , which is perpendicular to \mathbf{P} , deviates from $[1\ 1\ 0]$. For \mathbf{M}_c , the x and y components are oscillating to $-x$ and $+y$ directions initially. However, because of the right-handed relation governing \mathbf{D} , \mathbf{N} , and \mathbf{M}_c , \mathbf{M}_c rotates back to the initial direction. Therefore, both \mathbf{D} and \mathbf{N} switch 180° after polarization reversal while \mathbf{M}_c remains non-switched. Note that the driving force for magnetic switching during the polarization reversal comes from the magnetoelectric coupling including the rotation of bulk anisotropy energy and the \mathbf{H}_{DMI} . Besides, since BiFeO₃ is a G-type antiferromagnet with weak magnetization, the demagnetization energy is negligible compared to that of a ferromagnet. Hence, the damping precession is suppressed, and the switching speed becomes faster. If we look at the trajectories of \mathbf{N} switching, it is interesting that the switching trajectories of \mathbf{N} only lies on the xy plane and thus, \mathbf{N} switches much faster with less precession or oscillation compared to the magnetic movement of a ferromagnet.

Next, we look at the simulation results when the DM interaction is calculated using a spin Hamiltonian instead of a magnetic field (Figure 5). It can be seen that the switching curves obtained from the numerical micromagnetic model with the DMI spin Hamiltonian and OOMMF

using an effective magnetic field representing the DM field match well. Our findings contradict the results from the first principle calculations in ²², which indicates that \mathbf{M}_c switches but \mathbf{N} does not after polarization reversal. However, both of these scenarios are consistent with literature¹ in BiFeO₃/CoFe heterojunction which only track the easy axis of BiFeO₃ remains unchanged after polarization switching. In fact, in our simulations we also see cases in which \mathbf{M}_c switches and \mathbf{N} does not if the polarization switches very fast as will be shown in the later discussion. From our numerical micromagnetic model, we can obtain the spatial distribution of the effective magnetic field in each sublattice. In Figure 6 one can see that $\mathbf{H}_{ex,ij}$, $\mathbf{H}_{ani,bulk}$, and $\mathbf{H}_{dem,i}$ are staggered fields, while \mathbf{H}_{DMI} is a uniform field. The reason for a uniform DM field is because the magnetization and $\mathbf{D}_{i,j}$ are both staggered vectors. Hence, we believe that the cross product of them can be approximated as an effective magnetic field as we have done in our OOMMF model. For an antiferromagnet, a staggered field creates a precessing torque on Neel vector while a homogeneous field cants the magnetic moment without reorienting the Neel vector if the magnetic field does not reach spin-flop transition field³², which is consistent with our results.

We then evaluate the theoretical antiferromagnetic switching time of a single-domain BiFeO₃ thin film from switching time of \mathbf{N} for various hypothetical polarization switching times. In previous experiments, it has been reported that increasing the magnitude of the electric field in (100) BiFeO₃ thin film improved the polarization switching time from second to microsecond¹⁶. However, those experiments involved very large samples size (~area of 750 μm^2 and thickness of 300 nm) and the parasitics of the sensing circuits were quite dominant³³. We analyze the switching time of \mathbf{N} with the varying polarization switching time T_{FE} from 10 ps to 1 ns in Figure 7. The results show that the switching time of \mathbf{N} is proportional to T_{FE} , and in general, is longer than T_{FE} . In addition, when the polarization switching time is as fast as 10 to 20 ps, the spin vectors in the antiferromagnet cannot respond and \mathbf{N} remains non-switched whereas \mathbf{M}_c switches, which corresponds to a switching failure of \mathbf{N} ; and if T_{FE} is larger than 30 ps, \mathbf{N} switches but \mathbf{M}_c does not switch. Therefore, 30 ps is theoretically calculated as the lower limit of the antiferromagnetic switching time of a BiFeO₃ thin film device when K_{AFM} is $-1.75 \times 10^4 \text{ J/m}^3$. We can also roughly calculate this minimum time of magnetization reorientation, or called magnetic relaxation time, using $\frac{1}{f} = \frac{2\pi}{\gamma H_{eff}} \approx 36 \text{ ps}$ where f is the ferromagnetic resonance frequency, and H_{eff} is the effective applied field, which is $H_{ani,bulk}$ in the case of BiFeO₃. So when T_{FE} is shorter than the magnetic relaxation time, \mathbf{N} cannot switch but the coupling between \mathbf{P} , \mathbf{N} , and \mathbf{M}_c then force \mathbf{M}_c to switch 180° after polarization reversal.

It is also important to know the critical parameters that affect the switching dynamics of BiFeO₃. To check the sensitivity of parameters, such as J_{AFM} , K_{AFM} , and K_{EPI} , the magnitude of these parameters are varied in the switching dynamics of an antiferromagnet. We find that when the exchange coupling field becomes smaller than $-2.6 \times 10^{-13} \text{ J/m}$, the switching trajectories of \mathbf{M}_c becomes highly oscillatory. This is because the deviation of spin vectors from their preferred axis increases under a weak exchange coupling as shown in Figure 8. In contrast to the case when the coupling is strong, the switching of \mathbf{N} fails and the switching time of \mathbf{M}_c increases because of the characteristics of oscillatory switching. Regarding to K_{AFM} and K_{EPI} , one needs to note that they both affect the magnitude of the energy barrier. However, K_{AFM} also affects the

driving force for magnetization switching because K_{AFM} originates from the DMI and is proportional to the polarization and the electric field. Thus, increasing K_{AFM} increase the effective field and the energy barrier of the AFM thus implies a higher switching success rate of \mathbf{N} under thermal noise, a shorter minimum input pulse width, and a shorter switching time because of a shorter period of oscillation. For the compressive constraint, increasing K_{EPI} affect the crystal structure of BiFeO_3 to be more tetragonal-like and magnetic moments to lie in-plane. To have a successful and faster Neel vector switching, it is important to increase the magnitude of K_{AFM} and K_{EPI} for sufficient energy barrier to alleviate the thermal noise effect and also reduce the relaxation time of BiFeO_3 .

Conclusion

We have analyzed the switching dynamics of a single-domain BiFeO_3 thin film by solving LK and LLG equations, simultaneously. Our results show that BiFeO_3 as a G-type antiferromagnet has staggered spin vectors thus staggered DM vector, which creates a weak magnetization by tilting spin vectors unidirectionally. From the analysis of the energy landscape, we also demonstrate that the preferred axis of the magnetic moment in BiFeO_3 is determined by both the bulk DMI energy that couple to polarization and the epitaxial strain that comes from substrate. We then show for the first time that \mathbf{N} rotates 180° while \mathbf{M}_c remains unchanged by rotating polarization 180° and verify the results by solving the effective equation of motion for the Neel vector in the LG theory. The driving force of the magnetic switching is due to the magnetoelectric coupling such that the easy plane state and \mathbf{H}_{DMI} rotate along with the polarization. By checking the sensitivity of the parameters, we find that the probability of switching of \mathbf{N} depends not only by the anisotropy energy barrier but also on the exchange coupling field in BiFeO_3 . We further calculate the lower limit of the switching time of BiFeO_3 to be around 30 ps assuming the polarization can be switched as fast. \mathbf{N} cannot be switched if the polarization switches faster than 30 ps. The results shown in this paper are of importance to justify BiFeO_3 as a promising material for fast voltage-controlled devices such as magnetic-random-access memory and ME beyond-CMOS logic.

Table 1 Simulation parameter in the ferroelectric dynamics model ²³

Variable	Value	Units (SI)
P_s	0.8	Cm^{-2}
α_1	$4.9(T-1103) \times 10^5 = -3.935 \times 10^8$ when $T=300$ K	$C^{-2}m^2N$
α_{11}	6×10^8	$C^{-4}m^6N$
α_{12}	-1×10^6	$C^{-4}m^6N$
γ_{FE}	5×10^{-3}	$msec/F$
K_{Strain}	6×10^8	N/m^2
ϵ_r	54	—
E_{ext}	3×10^8	V/m

Table 2 Simulation parameters in the magnetic dynamics model

Variable	Value	Units (SI)
M_s	4.26×10^5	A/m
K_{AFM}	-1.75×10^4	J/m^3
K_{EPI}	-1.75×10^4	J/m^3
A_{AFM}	-2.6×10^{-12}	J/m
H_{DMI}	1000	Oe
α	0.01	—
γ	2.21×10^5	$(A/m)^{-1}s^{-1}$

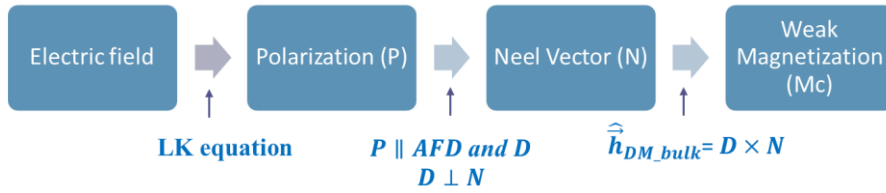


Figure 1 Strategies of the ferroelectric and micromagnetic simulation model of $BiFeO_3$

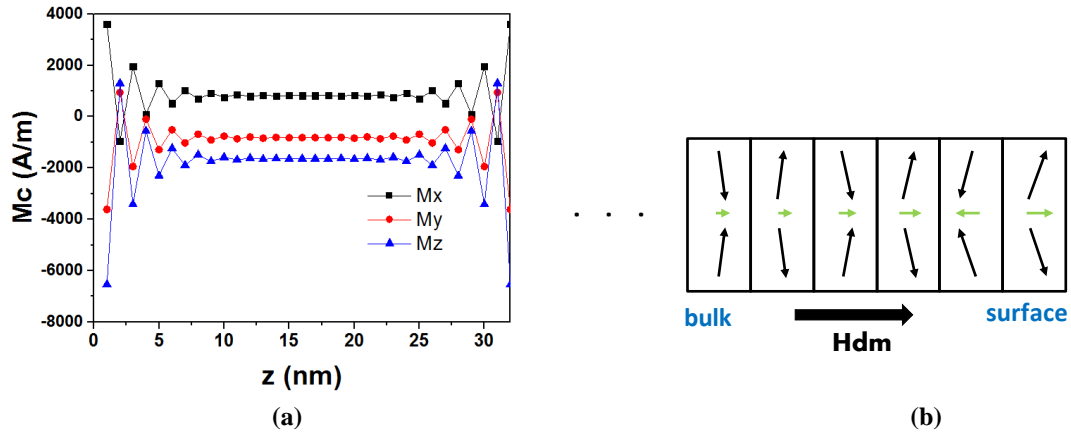


Figure 2 (a) M_c in 32 nm AFM with $H_{DMI}=1000$ Oe. (b) Schematic of magnetic moments inside a 1D antiferromagnet array under weak DM field. The black arrows represent the spin vectors and the green arrows represent the direction of M_c .

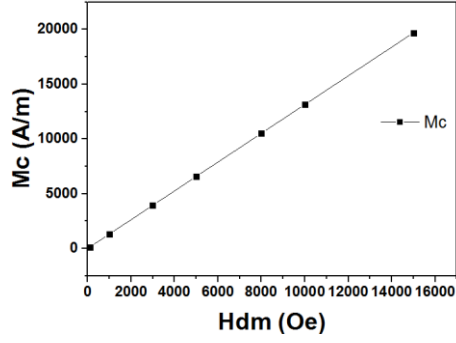


Figure 3 A 32 nm BiFeO₃ thin film, $K_{AFM} = K_{EPI} = -1.75 \times 10^4 \text{ J/m}^3$

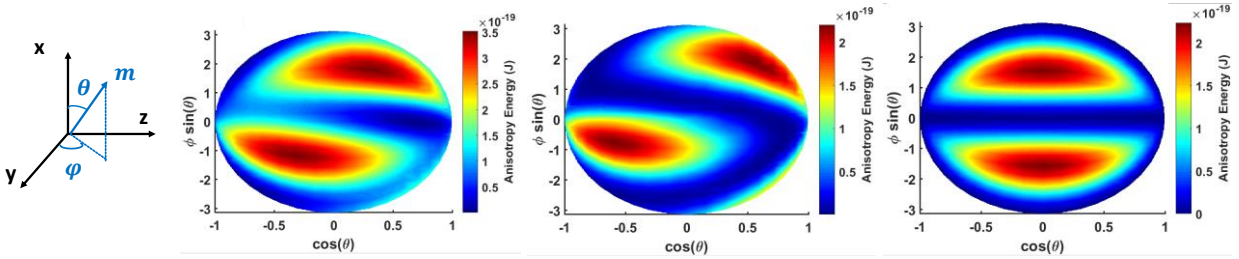


Figure 4 Energy landscape of BiFeO₃ thin film when (a). $K_{AFM}=K_{EPI}=-1.75 \times 10^4 \text{ J/m}^3$ (b). $K_{AFM}=-1.75 \times 10^4 \text{ J/m}^3$ and (c). $K_{EPI}=-1.75 \times 10^4 \text{ J/m}^3$

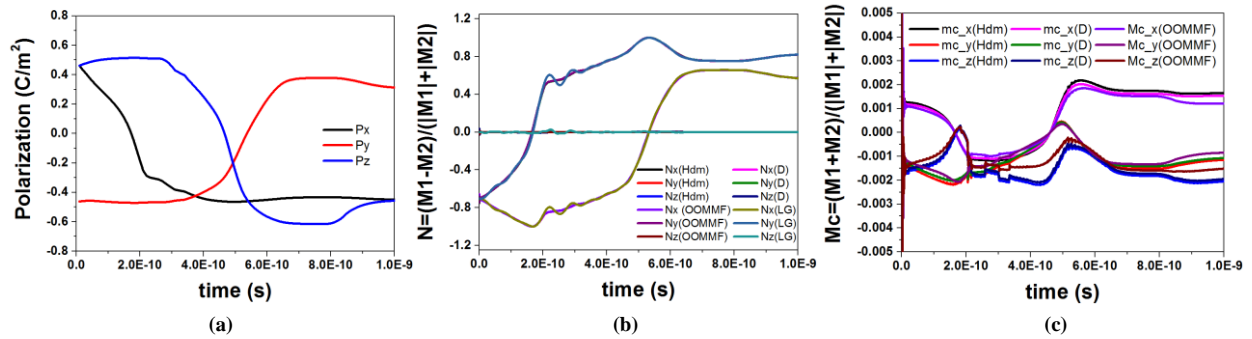


Figure 5 Switching dynamics of (a). polarization, (b). Neel vector, and (c). weak magnetization in 10 nm BiFeO₃ thin film with $K_{AFM}=K_{EPI}=-1 \times 10^6 \text{ J/m}^3$ and $H_{DMI} = 1000 \text{ Oe}$ simulated by OOMMF, MATLAB where DMI is an effective magnetic field (Hdm) or from spin Hamiltonian (D), and LG theory.

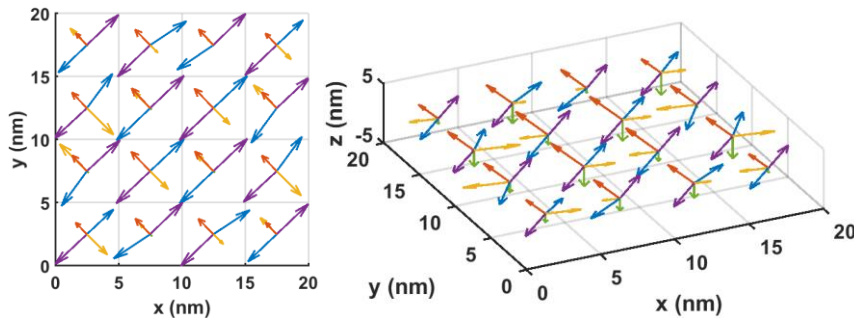


Figure 6 Spatial distribution of Heff including H_{ex} (violet), $H_{ani,bulk}$ (yellow), $H_{ani,epi}$ (green), H_{dem} (blue), and H_{DMI} (red) in AFM with $z=1 \text{ nm}$.

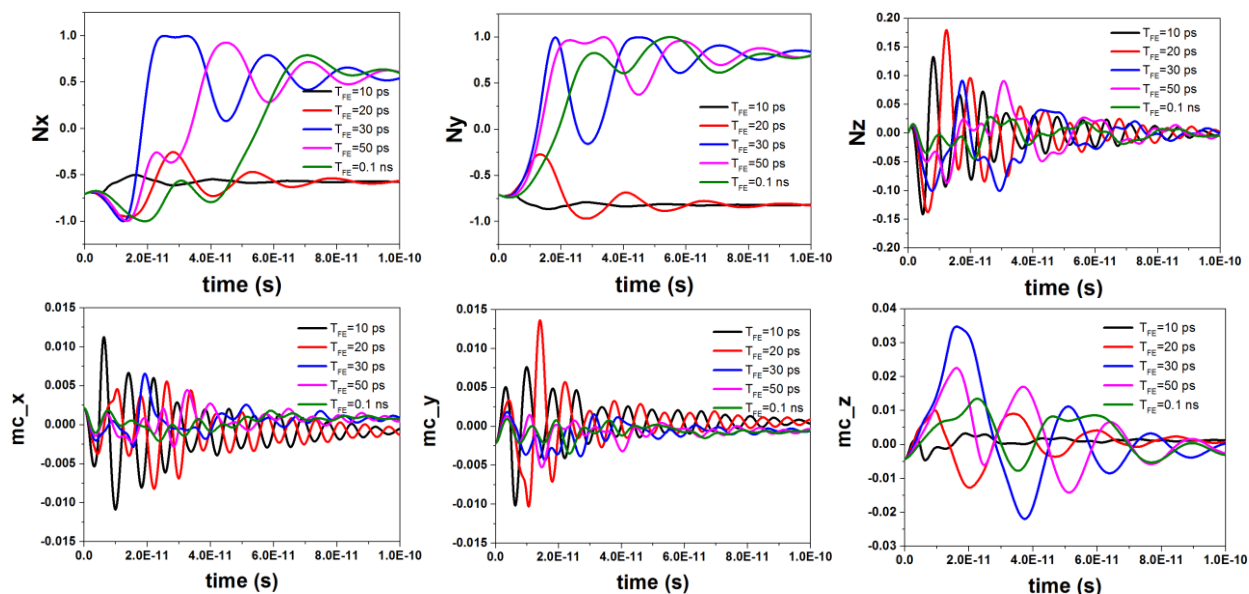


Figure 7 Switching curves of BiFeO_3 thin film with varying T_{FE}

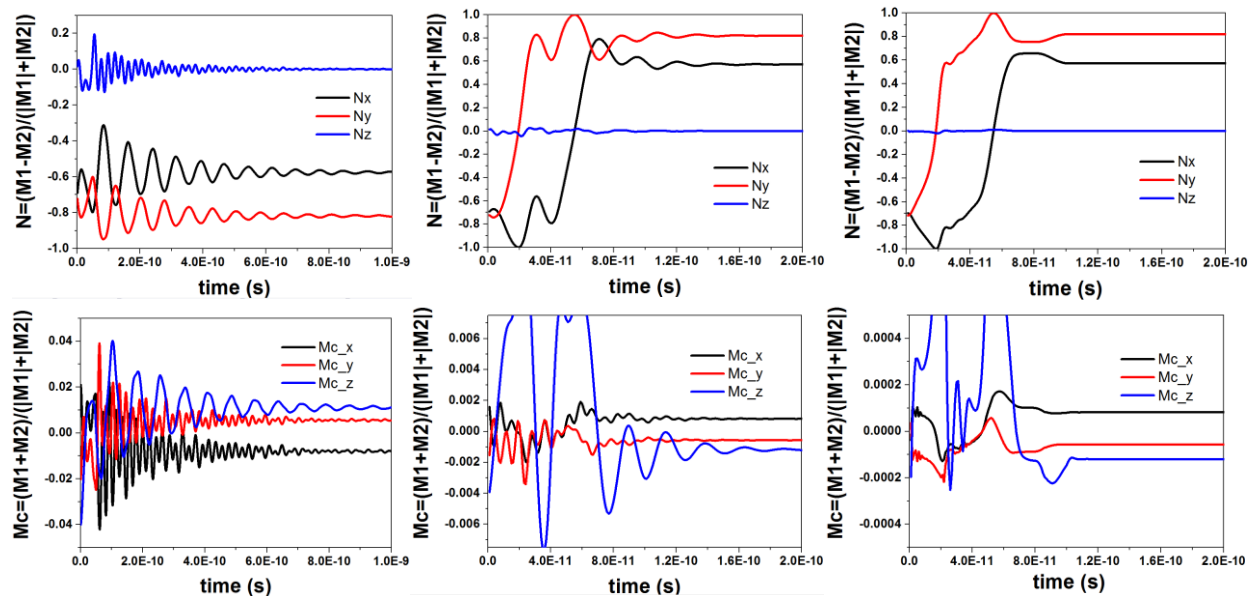


Figure 8 The switching dynamics of Neel vector and M_c of the BiFeO_3 thin film with $J_{AFM} = -0.26 \text{ pJ/m}$, -2.6 pJ/m , and -26 pJ/m (left to right)

References

1. Heron, J. T. *et al.* Deterministic switching of ferromagnetism at room temperature using an electric field. *Nature* **516**, 370–373 (2014).
2. Ruetter, B. *et al.* Magnetic-field-induced phase transition in BiFeO₃ observed by high-field electron spin resonance: Cycloidal to homogeneous spin order. *Phys. Rev. B - Condens. Matter Mater. Phys.* **69**, (2004).
3. Nikonov, D. E. & Young, I. A. Overview of beyond-CMOS devices and a uniform methodology for their benchmarking. *Proc. IEEE* **101**, 2498–2533 (2013).
4. Manipatruni, S., Nikonov, D. E. & Young, I. A. Beyond CMOS computing with spin and polarization. *Nat. Phys.* (2018). doi:10.1038/s41567-018-0101-4
5. Nikonov, D. E. & Young, I. A. Benchmarking of Beyond-CMOS Exploratory Devices for Logic Integrated Circuits. *IEEE J. Explor. Solid-State Comput. Devices Circuits* **1**, 3–11 (2015).
6. Nikonov, D. E. & Young, I. A. Benchmarking spintronic logic devices based on magnetoelectric oxides. *J. Mater. Res.* **29**, 2109–2115 (2014).
7. Schmid, H. Multi-ferroic magnetoelectrics. *Ferroelectrics* **162**, 317–338 (1994).
8. Cheng, R., Daniels, M. W., Zhu, J.-G. & Xiao, D. Ultrafast switching of antiferromagnets via spin-transfer torque. *Phys. Rev. B* **91**, 64423 (2015).
9. Roy, P. E., Otxoa, R. M. & Wunderlich, J. Robust picosecond writing of a layered antiferromagnet by staggered spin-orbit fields. *Phys. Rev. B* **94**, 14439 (2016).
10. Kimel, A. V. *et al.* Inertia-driven spin switching in antiferromagnets. *Nat. Phys.* **5**, (2009).
11. Heron, J. T. *et al.* Electric-field-induced magnetization reversal in a ferromagnet-multiferroic heterostructure. *Phys. Rev. Lett.* **107**, (2011).
12. Zhou, Z. *et al.* Probing electric field control of magnetism using ferromagnetic resonance. *Nat. Commun.* **6**, 1–7 (2015).
13. Qiu, D. Y., Ashraf, K. & Salahuddin, S. Nature of magnetic domains in an exchange coupled BiFeO₃/CoFe heterostructure. *Appl. Phys. Lett.* **102**, (2013).
14. Wang, J. J. *et al.* Magnetization reversal by out-of-plane voltage in BiFeO₃-based multiferroic heterostructures. *Sci. Rep.* **5**, 1–13 (2015).
15. Sando, D. *et al.* Crafting the magnonic and spintronic response of BiFeO₃ films by epitaxial strain. *Nat. Mater.* **12**, (2013).
16. Pantel, D. *et al.* Switching kinetics in epitaxial BiFeO₃ thin films. *J. Appl. Phys.* **107**, 84111–21303 (2010).
17. Yang, Y., Infante, I. C., Dkhil, B. & Bellaiche, L. Strain effects on multiferroic BiFeO₃ films. *Comptes Rendus Phys.* **16**, 193–203 (2015).
18. J. T. Heron, D. G. Schlom, and R. R. Electric Field Control of Magnetism Using Multiferroic Bismuth Ferrite. *J. Japan Soc. Powder Powder Metall.* **61**, S19–S24 (2014).
19. Dzyaloshinsky, I. Thermodynamic Theory of ‘Weak’ Ferromagnetism In Antiferromagnetic Substances. *Sov. Phys. JETP* **5**, 1259–1272 (1957).

20. Moriya, T. Anisotropic superexchange interaction and weak ferromagnetism. *Phys. Rev.* **120**, 91–98 (1960).
21. Zvezdin, A. K. &Pyatakov, A. P. On the problem of coexistence of the weak ferromagnetism and the spin flexoelectricity in multiferroic bismuth ferrite. *EPL* **99**, (2012).
22. Ederer, C. &Spaldin, N. A. Weak ferromagnetism and magnetoelectric coupling in bismuth ferrite. *Phys. Rev. B* **71**, 060401 (2005).
23. Zhang, J. X. *et al.* Effect of substrate-induced strains on the spontaneous polarization of epitaxial thin films Ferroelectric size effects in multiferroic thin films Phase-field model of domain structures in ferroelectric thin films. *J. Appl. Phys. Lett.* **101**, 114105–51606 (2007).
24. Agbelele, A. *et al.* Strain and Magnetic Field Induced Spin-Structure Transitions in Multiferroic BiFeO₃. *Adv. Mater.* **29**, 1–8 (2017).
25. Hals, K. M. D., Tserkovnyak, Y. &Brataas, A. Phenomenology of current-induced dynamics in antiferromagnets. *Phys. Rev. Lett.* **106**, (2011).
26. Gomonay, H.V &Loktev, V. M. Spin transfer and current-induced switching in antiferromagnets. *Phys. Rev. B* **81**, 144427 (2010).
27. M.J. Donahue and D.G. Porter. OOMMF User’s Guide, Version 1.0 Interagency Report NISTIR 6376, National Institute of Standards and Technology, Gaithersburg, MD (Sept 1999). Available at: <http://math.nist.gov/oommf/>.
28. Miltat, J. E. &Donahue, M. J. Numerical Micromagnetics: Finite Difference Methods. *Handb. Magn. Adv. Magn. Mater.* 1–23 (2007). doi:10.1002/9780470022184
29. Zhao, T. *et al.* Electrical control of antiferromagnetic domains in multiferroic BiFeO₃ films at room temperature. *Nat. Mater.* **5**, 823–829 (2006).
30. Bé, H. *et al.* Structural distortion and magnetism of BiFeO₃ epitaxial thin films: A Raman spectroscopy and neutron diffraction study. *Philos. Mag. Lett.* **87**, 3–4
31. Matsuda, M. *et al.* Magnetic dispersion and anisotropy in multiferroic BiFeO₃. *Phys. Rev. Lett.* **109**, (2012).
32. Jungwirth, T., Marti, X., Wadley, P. &Wunderlich, J. Antiferromagnetic spintronics. *Nature Nanotechnology* **11**, 231–241 (2016).
33. Li, J. *et al.* Ultrafast polarization switching in thin-film ferroelectrics. *Appl. Phys. Lett.* **84**, 1174–1176 (2004).